RESEARCH ARTICLE

Open Access

A Through-Intact-Skull (TIS) chronic window technique for cortical structure and function observation in mice

Dongyu Li[1,2†], Zhengwu Hu[1†], Hequn Zhang[3,4], Qihang Yang[1], Liang Zhu[3,4], Yin Liu[4], Tingting Yu[1,2], Jingtan Zhu[1,2], Jiamin Wu[5], Jing He[5], Peng Fei[6], Wang Xi[4*], Jun Qian[3*] and Dan Zhu[1,2*]

Abstract

Modern optical imaging techniques provide powerful tools for observing cortical structure and functions at high resolutions. Various skull windows have been established for different applications of cortical imaging, and each has its advantages and limitations. Most critical of the limitations, none of the current skull windows is suitable for observing the responses to some acute craniocerebral injuries on a large scale and at high resolution. Here, we developed a "Through-Intact-Skull (TIS) window" that enables the observation of an immune response on a bilateral cortical scale and at single-cell resolution after traumatic brain injury without affecting the pathological environment of the brain. The TIS window also has the advantages of craniotomy-freeness, centimeter-field of view, synaptic resolution, large imaging depth, long-term observation capability, and suitability for awake mice. Therefore, the TIS window is a promising new approach for intravital cortical microscopy in basic research in neuroscience.

Keywords: Skull optical clearing window, Long-term neurovascular imaging, Traumatic brain injury, Awake animal

1 Introduction

In vivo brain observation at high resolution is fundamental to understanding its physiological function and studying the internal mechanism, pathogenesis and potential treatment of various brain-related diseases [1–3]. Modern optical imaging techniques provide powerful tools for observing cortical structure and functions at high resolutions and low invasiveness, making it possible to track changes in healthy or pathological brains in vivo [4–6]. However, the scattering of the turbid skull during procedures severely affects light penetration, limiting imaging quality and depth in the cortex [7, 8]. Therefore, in vivo cortical optical imaging typically requires assistance from "skull windows".

The open-skull glass window and thinned-skull window are the two most widely used skull window techniques [9, 10]. The open-skull glass window requires the skull to be removed and the brain to be covered with a transparent glass slide [11–13] that is capable of long-term observation over months [14, 15], among which a curved glass window can provide optical access to an estimated 800,000–1,100,000 individual neurons across the dorsal surface of neocortex [16]. For the thinned-skull window, the partial skull is ground extremely thin (< 25 μm) to allow light penetration [17–19]. In addition to these two surgery-based

---

[†]Dongyu Li and Zhengwu Hu contributed equally to this work

*Correspondence: xw333@zju.edu.cn; qianjun@zju.edu.cn; dawnzh@mail. hust.edu.cn

[1] Britton Chance Center for Biomedical Photonics - MoE Key Laboratory for Biomedical Photonics, Wuhan National Laboratory for Optoelectronics - Advanced Biomedical Imaging Facility, Huazhong University of Science and Technology, Wuhan 430074, Hubei, China
[3] State Key Laboratory of Modern Optical Instrumentations, Centre for Optical and Electromagnetic Research, College of Optical Science and Engineering, International Research Center for Advanced Photonics, Zhejiang University, Hangzhou 310058, China
[4] Interdisciplinary Institute of Neuroscience and Technology, Department of Anesthesiology, The Second Affiliated Hospital, School of Medicine, Zhejiang University, Kaixuan Road 258th, Hangzhou 310020, China
Full list of author information is available at the end of the article

skull windows, chemical agent-based skull windows capable of rendering the skull more transparent to light have been developed in recent years: "Transparent skull window" and "skull optical clearing window" are two representative agent-based techniques [20–23].

Regrettably, none of these skull windows is adequate for large-scale high-resolution continuous observation of some acute brain disease models. For example, the open-skull glass window approach is not appropriate for in vivo high-resolution optical brain imaging of acute traumatic brain injury (TBI), which is caused by external forces and is common during both peace and war [24, 25], occurring in an estimated 69 million patients worldwide each year [26], because it will inevitably change intracranial pressure, altering the native state of the brain, and is not suitable for immediate imaging of brain recovery [10, 27]. The thinned-skull window is more well-suited for examining real responses in specific pathological states right after TBI; however, it only enables the observation of a small area because it is incapable of evenly polishing a large area of the skull to 25 μm [28–30] or determining the occurrence of responses across brain regions without a global field of view. Although transparent skull window and skull optical clearing window can provide centimeter-scale fields of view without craniotomy, the former does not grant the single-cell tracking of intracranial immune responses due to its limited transparency, while the latter cannot ensure continuous observation because the agents need to be supplied frequently, which would interrupt the observation, while and the immune response process often lasts several hours or longer [31, 32].

Therefore, developing a skull window technique capable of simultaneously meeting requirements, including maintenance of the internal environment and provision of a wide field of view, high resolution, and durability, and offering a tool for various physiological and pathological studies, is pivotal.

In this research, we established a chronic skull optical clearing window named "Through-Intact-Skull window (TIS window)" without craniotomy in mice. It is the first window to provide a bilateral cortical field of view for tracking immune responses to acute TBI at single-cell resolution. In addition, the imaging scale, resolution power, work time, and ability to image awake mice under the TIS window were evaluated, and findings showed that it could also be used in the most applications those current skull windows were suitable for. Therefore, the novel technology can be used in various applications of in vivo cortical visualization and holds great potential in brain science investigations.

2 Results
2.1 TIS window for continuous observation on a centimeter-scale and at single-cell resolution after TBI

The main components of bone consist of calcium hydroxyapatite (16%), collagen (16%), lipids (54%), and water (14%) [33]. To establish a long-term TIS window, 3 agents were used here, named S1, S2 and S3 and were used to remove collagen, remove lipids and match refractive index (RI), respectively. S1 is a saturated supernatant solution of 75% (vol/vol) ethanol and urea, the hydroxyl groups in which could dissolve the collagen. S2 is a high-concentration sodium dodecylbenzenesulfonate solution, which is used as a degreasant. S3 is a UV-curable adhesive, which has a high RI of 1.5 for RI match. The unique advantage of TIS window over previous skull optical clearing windows was brought about by S3. The existed skull optical clearing agents are liquid based [20, 23, 34, 35], which is hard to remain on the skull when the mice recovered to move freely, thus the optical clearing treatment to the skull is needed every time before imaging, making it rather inconvenient. On the contrary, after UV irradiation, S3 can be cured and kept relatively still against the skull, therefore make the skull stay transparent for a long time even during the movement of mice. Moreover, the UV-curable adhesive as a higher RI over most of the water-soluble reagent, thus has better refractive index matching effect.

The established TIS window remarkably decreased the degree of scattering of the skull, making it transparent (Additional file 1: Fig. S1), thus improving in vivo cortical imaging quality (Additional file 1: Fig. S2). Through the TIS window, immune cell movements were monitored on a bilateral cortical scale after TBI using a fluorescent stereomicroscope. As shown in Fig. 1a and Additional file 2: Video S1, the TIS window provided a centimeter-field of view for single-cell-resolution observation, which revealed that not only did neutrophils appear near the injury area of the mouse after the occurrence of TBI but neutrophil movements were also registered far away from the injury center, even on the opposite side of the injury, with no movement noted across regions, suggesting that TBI possibly causes a whole-cortex multi-location immune response instead of a local response only.

Additionally, we identified and tracked neutrophils in three ROIs after TBI (Fig. 1b–j). As seen in Fig. 1k–n, the tracked neutrophils in ROI 1 gathered predominantly around the trauma area but far from the midline; the tracked neutrophils in ROI 2 occurred primarily near the trauma area and close to the midline; the tracked neutrophils in ROI 3 appeared contralaterally to the trauma area. We examined the cytodynamics based on

these three ROIs (Fig. 1o–r) and noted more neutrophils on the injured side, as well as more significant distance, velocity, displacement, and speed of movement than on the contralateral side. Moreover, the distance from the midline seemed to more considerable affect the intensity of neutrophil movement compared to the distance from the injury center, and the closer the velocity was to the midline, the faster it was. Also, the number of neutrophils in the vicinity of the injury area increased gradually over several hours of continuous observation (Additional file 1: Fig. S3).

Furthermore, bleeding occasionally occurred after TBI (sometimes not), but not necessarily immediately (Additional file 3: Video S2 and Additional file 4: Video S3), and not solely in the vicinity of the injury. As shown in Fig. 1s and Additional file 3: Video S2, there was no palpable bleeding in the cortex at the beginning of the observation (1 h post-TBI). However, 1 h later (2 h post-TBI), sudden hemorrhaging was apparent near the site of injury, rapidly spreading to the suture and accompanied by spasms throughout the cortex. Over the next few hours, the bleeding slowly disappeared. Through the TIS window, we perceived an area of immune response away from the injury site and quantified the velocity of movement of immune cells in this area. The results revealed that immune cell activity slowly increased after bleeding, peaked as the bleeding spread to the area, and then dropped off very quickly and no longer fluctuated as much (Fig. 1u).

2.2 TIS window for centimeter-scale synaptic resolution imaging

The maximum imaging scale and imaging resolution through the TIS window were evaluated using two-photon microscopy (2PM) to record cortical vasculature and neurons. Figure 2a1 demonstrates the performance of dual-channel neurovascular two-photon microscopy through a dual-hemispheric TIS window. Both large blood vessels and tiny microvasculature in the cortex were distinctly visualized. Observing cortical areas

around the sutura using the open-skull glass window is problematic because removing the skull above these areas can cause massive bleeding. In contrast, viewing the areas around the sutura using the TIS window without fear of causing bleeding was easy (Fig. 2a2–a4) and resulted in the identifiable observation of dendritic spines (Fig. 2a5–a10).

We next visualized neuronal morphology and structure and compared the image quality and achievable imaging depths of the initial state skull, TIS window establishment and skull removal. As shown in Fig. 2b, details of the apical dendrites were hard to resolve through the original skull, even with their location on the surface of the cortex. High background signals obscured axons and cell bodies in deep tissues, and the profiles of the neurons were hardly distinguishable at 400-μm depth. However, through the TIS window, the apical dendrites, axons and cell bodies in the cortex were noticeable under two-photon microscopy, and the final imaging depth easily surpassed 500 μm, where the lateral resolution was still tolerable. Admittedly, the axial resolution power at a massive depth through the TIS window was lower than that through the open-skull glass window, therefore the 3-dimentional structure of the cell bodies at large depth could not be reconstructed as well as through the open-glass window (Additional file 1: Fig. S4). However, the resolution in a shallow layer through the TIS window was similar to that through skull-opened window (Fig. 2d and Additional file 1: Fig. S5), with a slightly lower resolution in the deep layer of over 500 μm (Additional file 1: Fig.S6).

The performance of the TIS window was also compared to those of two previous skull optical clearing window techniques. Relative to the Skull Optical Clearing Window technique (SOCW) [35] and Urea-based Skull Optical Clearing Agents (USOCA) [23], both the resolving power and imaging contrast of the TIS window were remarkably superior (Additional file 1: Figs. S7 and S8). Notably, the two-photon system used in this research was better than that applied in previous

(See figure on next page.)
Fig. 1 TIS window for bilateral cortical observation post-TBI. **a** Fluorescence imaging of a TBI mouse on a centimeter scale using a commercial fluorescence magnification microscope. The purple asterisk indicates the central location of the TBI. **b**–**d** Larger views of the three areas demarcated with box lines in (**a**). **e**–**g** The results of neutrophil and vessel segmentations in (**b**–**d**), respectively. **h**–**j** Tracked neutrophils in each ROI. The colors represent the average velocities of the various neutrophils. **k-l** The relationship between the travel distance and the distance to **k** the injury center or **l** the midline. **m**–**n** The relationship between the travel velocity and the distance to **m** the injury center or (n) the midline. **o**–**r** Quantitative analyses of neutrophil cytodynamics in three ROIs. Travel distance: the length of the path taken by a trajectory; Travel velocity: travel distance divided by the time of movement; Travel displacement: distance between the end point and start point of each track; Travel speed: travel displacement divided by the time of movement. **s** Fluorescence imaging of another TBI mouse showing bleeding across several hours of observation. The purple asterisk indicates the central location of the TBI. The red dotted box highlights the bleeding area. **t** Enlarged view of the area in the solid blue line box in (**s**). **u** Changes in the average velocity of neutrophils in the area during observation. t1 denotes when the bleeding started. t2 indicates when the bleeding spread to the area. The red zone marks a sudden acceleration in bleeding
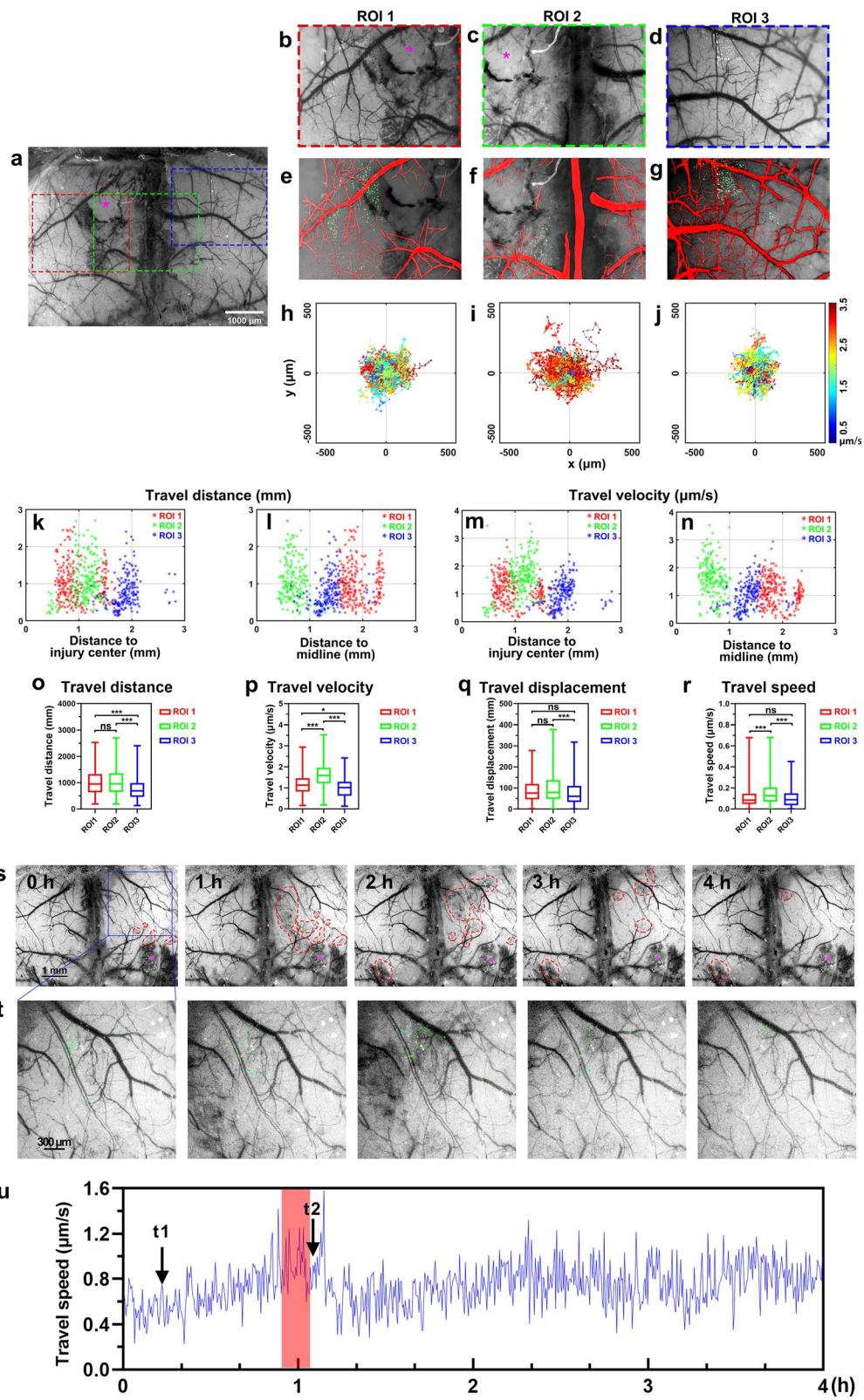
Fig. 1 (See legend on previous page.)

papers [23, 35]; therefore, the imaging depths of SOCW and USOCA here were greater than those reported previously.

2.3 TIS window for deep cortical imaging

To push the achievable imaging depth, we further evaluated our TIS window using the three-photon microscopy (3PM), which holds a key advantage of less out-of-focus backgrounds and, therefore, better signal-to-background ratios (SBR) in large tissue depths over the two-photon microscopy. Although three-photon microscopy uses a longer excitation wavelength than two-photon microscopy, thus allowing less scattering of tissues, the signal light in the short wavelength was still affected by tissue scattering monumentally. Therefore, without additional treatment, the through-skull three-photon neural imaging depth was markedly inferior to that obtained when the skull was removed [36, 37]. As such, evaluating the TIS window's ability to combine with three-photon microscopy to reach deeper tissues through an intact skull is vital.

Since two-photon imaging and three-photon imaging utilize different excitation wavelengths, assessing TIS window' compatibility with longer wavelengths needed for three-photon imaging is crucial [34]. As presented in Fig. 3a, Additional file 1: Fig. S9, and Additional file 5: Video S4 and Additional file 6: Video S5, three-photon microscopy enabled the perception of some information through the turbid skull at a certain depth, but few signals were perceptible below 400 μm. However, more synapses were notable in the superficial layer through the TIS window, and the imaging quality of several cell bodies in the deep layer (400–800 μm), which could not be monitored without the TIS window, was promising (Fig. 3b, c). The dendrites were distinguishable even at depths of 800–900 μm. In addition, the 3D shape of cell bodies was finely reconstructed (Fig. 3d), and the SBR at a bigger depth was still commendable (Fig. 3e). Given the results of the comparison between TIS window and open-skull glass window on two-photon microscopy, it is reasonable to assume that the three-photon imaging quality through

an open-skull glass window would be similar to that through the TIS window at shallow depth but slightly higher at large depth.

2.4 TIS window for long-term cortical vascular observation

To evaluate the ability of the TIS window to maintain skull transparency, we performed long-term monitoring of vasculature in the superficial and deep cortexes using two-photon microscopy imaging and laser speckle contrast imaging (LSCI). As shown in Fig. 4a, the TIS window enabled abundant high contrast monitoring of tiny microvasculature at the massive depth of 700 μm. Even 10 days after the TIS window establishment, the tiny microvasculature remained easily discernable with two-photon microscopy, and with an imaging depth as enormous as 900 μm.

In addition to structural observation, we demonstrated the capability of our TIS to aid in monitoring vascular function, such as blood flow velocity. As seen in Fig. 4b, through the TIS window, various blood flow profiles were measured at different depths. Additional file 1: Fig. S10 displays the results of the long-term LSCI observation across days 1–21 after the establishment of the TIS window. During the entire 2-week period, the skull remained transparent, and the contrast-to-noise ratio (CNR) of the cortical blood flow imaging quality was maintained at a high level (also see Additional file 1: Fig. S11). In the 3rd week, the CNR of LSCI reduced slightly, but all monitored blood vessels from the first two weeks were still distinguishable. This suggests that vascular function could be tracked for weeks with various imaging methods using the TIS window.

## 2.5 TIS window for long-term cortical neural observation

We next applied the TIS window to long-term monitoring of neurons in deep tissue at synaptic resolution using multi-photon microscopy. As shown in Fig. 5a, Additional file 1: Fig. S12 and Additional file 7: Video S6, the imaging quality and imaging depth of two-photon deep-tissue microscopy decreased negligibly over time, and axons were tracked down to a depth of 800 μm for 2 weeks after the TIS window establishment.

(See figure on next page.)
Fig. 2 TIS window for two-photon microscopy. **a1** A large-field and dual-channel two-photon microscopic image of bilateral hemispheric cortical blood vessels (in red, Texas red) and neurons (in green, EGFP) after the TIS window establishment (viewed with a 4 × objective). **a2**–**a4** High magnification images of the corresponding color frames in (a1) near the sutura (viewed with a 20 × objective). **a5-a10** High magnification (zoom in) images of the white frames (white arrow-indicated) in (**a2**–**a4**), respectively. (20 × objective, zoom 4). **b** Typical images of two-photon microscopy of neurons at various depths before and after the TIS window establishment, as well as after the removal of the skull. The axial step was set at 5 μm. **c** The SBRs of the images at various imaging depths under different conditions. The SBR was determined as follows: for each image of a certain imaging depth, firstly, a line across a typical structure (including the background around the structure) was drawn, and the intensity distribution along the line was obtained. Secondly, the obtained intensity values were normalized to 0–1. Thirdly, the ratio of the strongest value on the biological structure to the strongest value in the background was calculated as SBR. **d** Comparison between the TIS window and open-skull glass window in dendritic spine imaging. The excitation wavelength was 920 nm (80 MHz, 140 fs). Similar results were obtained in 4 mice
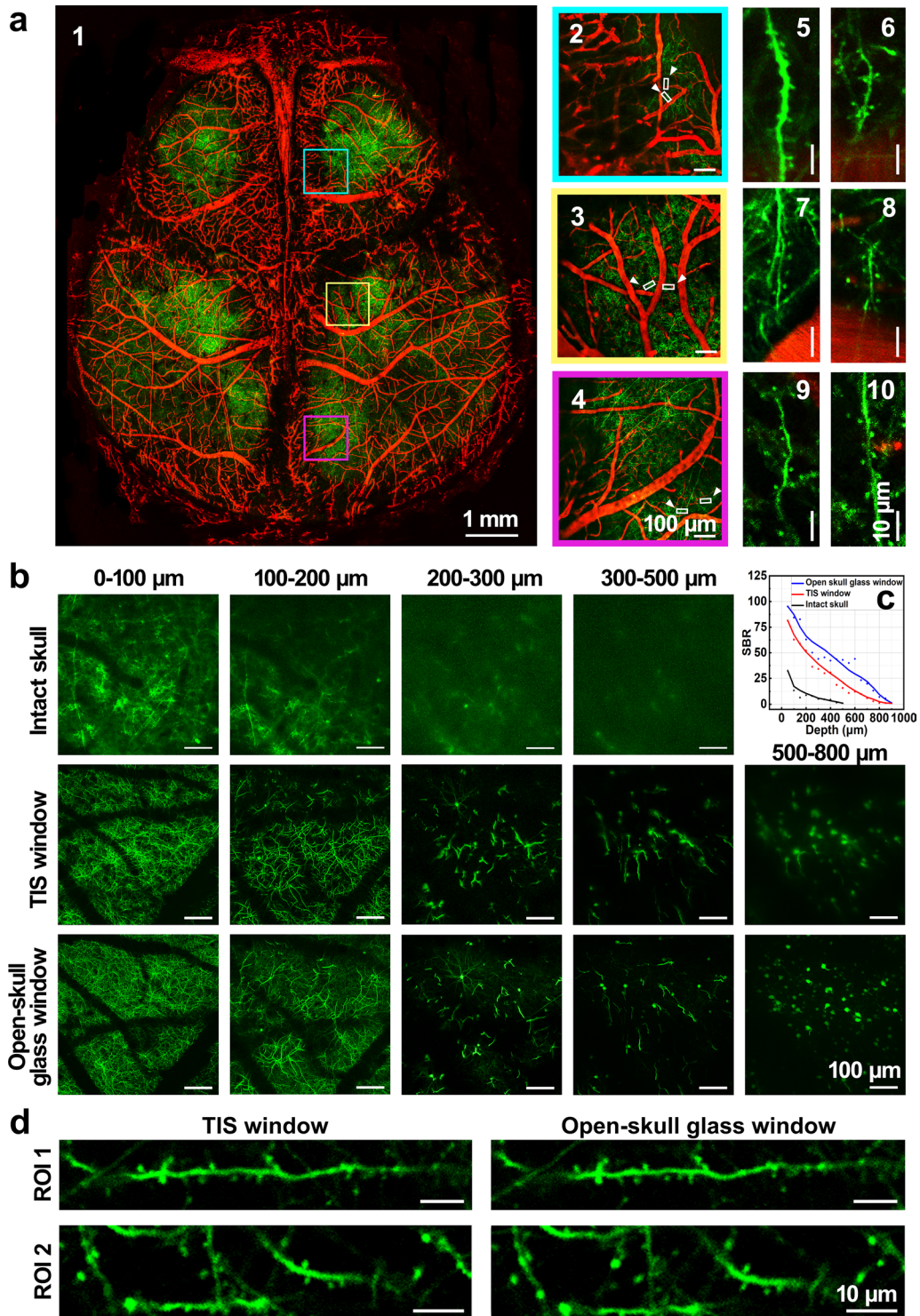
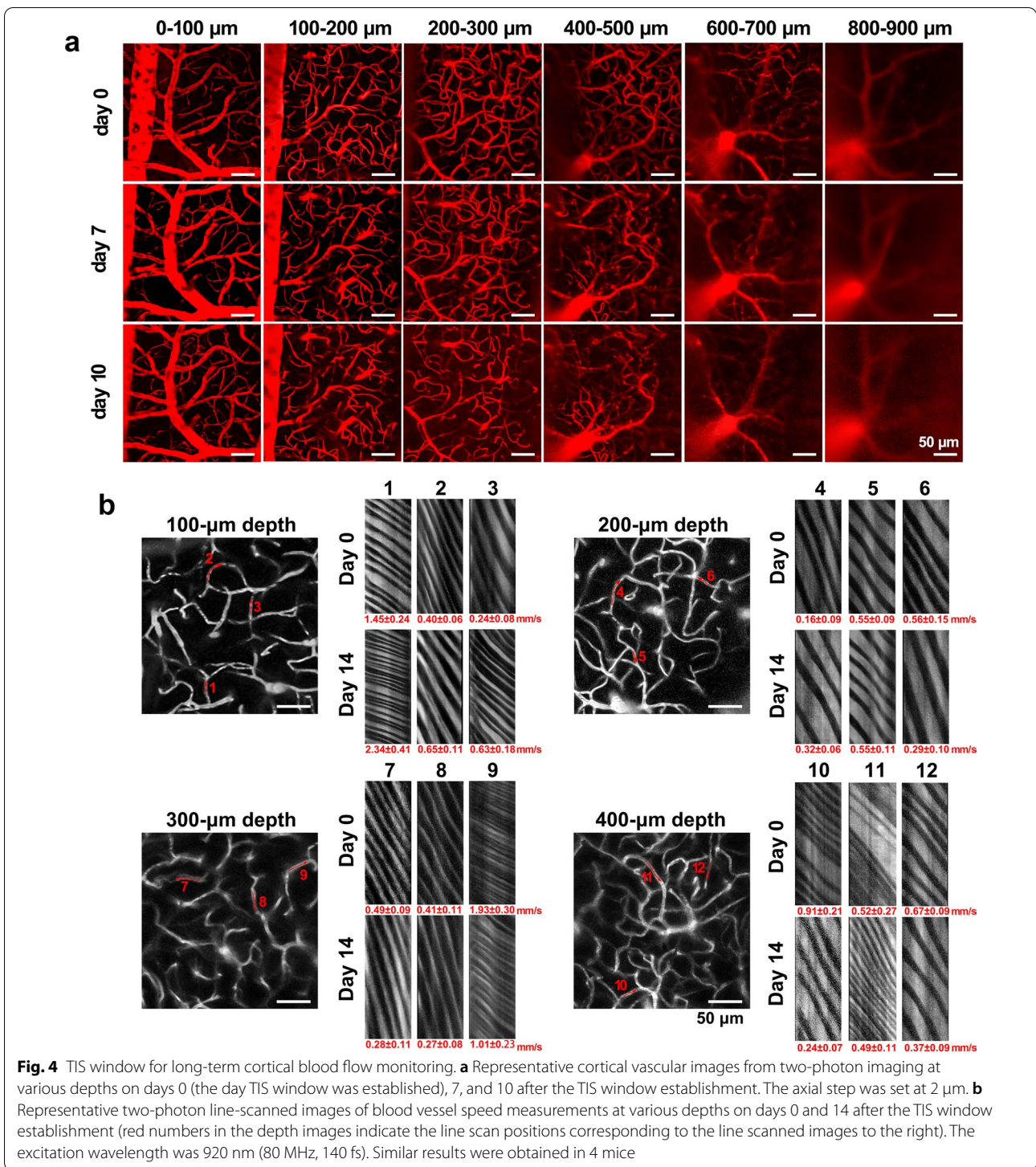**Fig. 2** (See legend on previous page.)
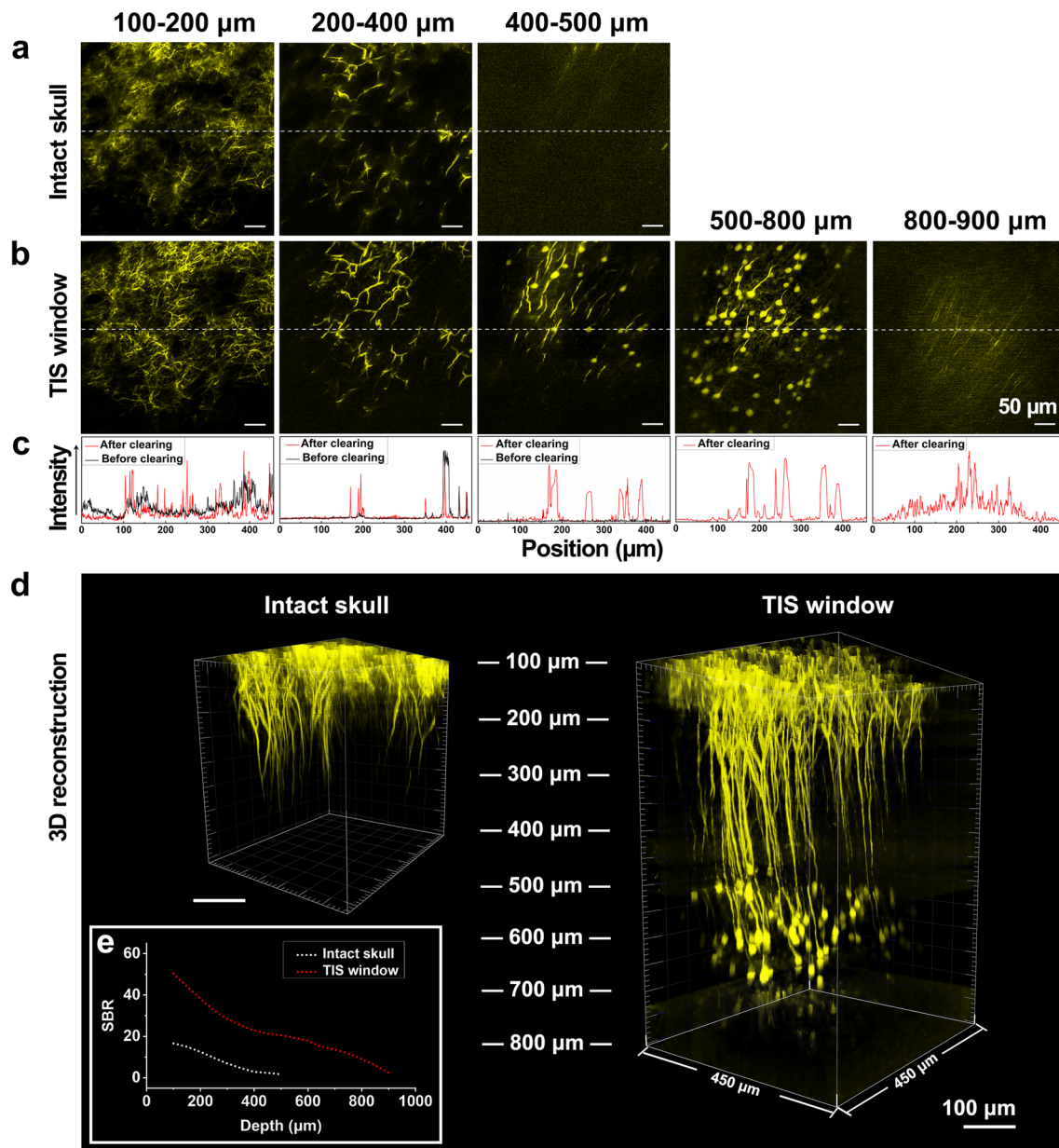
Fig. 3 TIS window for three-photon microscopy. **a, b** Representative images of the three-photon microscopy of neurons in a Thy1-YFP mouse at the 1300-nm excitation wavelength and at various depths before **a** and after **b** the TIS window establishment. **c** Signal intensity along the dashed lines in (**a**, **b**). **d** A 3D reconstruction image before and after the TIS window establishment. It was only achievable above 400 μm through an intact skull. **e** SBR at each depth before and after the TIS window establishment. The images were obtained using a 20 × objective; the excitation wavelength was 1300 nm (400 kHz, 50 fs); the axial step was set at 5 μm. Identical results were obtained in 3 mice

As seen in Fig. 6b, two-photon microscopy could not provide sufficient resolution for the observation of dendrites at the 150-μm depth or dendritic spines through an intact turbid skull. However, the long-term dynamics of spines were perceived reliably through the TIS window technique. The formation and elimination of dendritic spines were noted clearly over 10 days. This promising result shows that synaptic dynamics and their role in motor memories and neuronal circuit establishment, as well as brain dysfunctions, can be monitored using our technique [38, 39].

Figure 5c shows representative images of three-photon microscopy with visualizable dendritic spines, but at a lower resolution than with two-photon microscopy

Fig. 4 TIS window for long-term cortical blood flow monitoring. **a** Representative cortical vascular images from two-photon imaging at various depths on days 0 (the day TIS window was established), 7, and 10 after the TIS window establishment. The axial step was set at 2 µm. **b** Representative two-photon line-scanned images of blood vessel speed measurements at various depths on days 0 and 14 after the TIS window establishment (red numbers in the depth images indicate the line scan positions corresponding to the line scanned images to the right). The excitation wavelength was 920 nm (80 MHz, 140 fs). Similar results were obtained in 4 mice

(Fig. 5b), probably due to the slightly increased point spread function (PSF) at 1300 nm compared to 920-nm based two-photon microscopy. Still, three-photon microscopy holds the advantage of high resolution and high SBR in deep tissue and, thus, can be utilized to track

neural cell bodies. As presented in Fig. 5c, cell bodies at 500–700-µm depths were clearly visible through the TIS window for 10 days; however, these cell bodies were not distinguishable in 3D reconstruction using two-photon microscopy (Fig. 5a). Therefore, through the TIS window,

neurons from surface to deep cortex can be finely visualized long-term by combinedly employing two-photon and three-photon microscopy.

2.6 TIS window for long-term neural function imaging in awake mice

We next used the TIS window to monitor calcium-mediated neural activity in an awake mouse. As shown in Fig. 6a, the TIS window was established right after GCaMP6s virus injection and then left for 14 days. Figure 6b and Additional file 8: Video S7 display an ROI with 14 neuron dendrites during mouse paw movements. The screening of the spontaneous activity of each dendrite in the awake mouse through the TIS window was clear. Through the quick scanning imaging mode (24 fps), the TIS window enabled the distinction of dendrites at around 2 μm.

Neuronal activity in the somatosensory cortex was triggered via electro-stimulation (ES) of the forepaw. Figure 6c and Additional file 9: Video S8 depict an ROI with 21 neurons. Through the TIS window, most of the neurons demonstrated observable responses to ES from days 1 to 14 (Fig. 6c, d). These data suggest that the same neuron population activity can be tracked for weeks through the TIS window under two-photon imaging.

2.7 Biosafety assessment of the TIS window

While the long-term repeated imaging of neurons and blood vessels in the same positions without morphological changes, as shown in Figs. 4 and 5, suggested the absence of severe damage or toxicity thanks to our TIS window or the multi-photon microscopy, we additionally performed both in vivo and ex vivo experiments to further assess the biosafety of our method.

First, we monitored microglia in vivo 1 and 48 h after the TIS window establishment. The microglia remained at the same position and in an inactive state (Additional file 1: Fig. S13a), indicating that the TIS window does not trigger microglial activation.

Next, we conducted a series of ex vivo experiments. As shown in Additional file 1: Fig. S13b, the microglia perceived in both the TIS window and control hemisphere remained non-active with a highly branched morphology; the volume and ellipticity were not significantly

different in the two parts of the hemisphere. In addition, the GFAP immunofluorescence images demonstrate similar intensity and distribution in both sites (Additional file 1: Fig. S13c), implying that astrocytes were not activated. Furthermore, H&E-stained imaging uncovered no difference in the brain parenchyma between the TIS window and the contralateral visualization (Additional file 1: Fig. S14), suggesting that the TIS window does not cause inflammation.

As shown in Figs. 2, 3, 4 and 5, under the imaging condition as we used for two/three photon visualization (80 MHz, 10–100 mW for two-photon imaging and 400 kHz, 5–50 mW for three-photon imaging), we monitored cortical blood vessels and neurons for weeks and did not observe any injury or dysfunctions, suggesting there is no obvious phototoxicity of the combination of TIS window and such optical imaging techniques. In addition, we used two-photon microscopy to further evaluate the laser damage threshold through TIS window. During the normal imaging processing, the laser power was adjusted from 10 mW (at surface) to 100 mW (deeper than 600 μm). Firstly, 250 mW was used to focus on the cortex at the depth of 700 μm through TIS window to evaluate if it will damage the surface since the power would be higher there. As shown in Additional file 1: Fig. S15a, the dendritic structure showed no change after continuous irradiation. Secondly, different laser power was used to focus on the brain surface through TIS window. As shown in Additional file 1: Fig. S15b, the dendrites began to appear beaded when the laser power reached 150 mW, 15 times as high as the two-photon imaging required. Such results indicates that the TIS window is safe with the respect of photodamage.
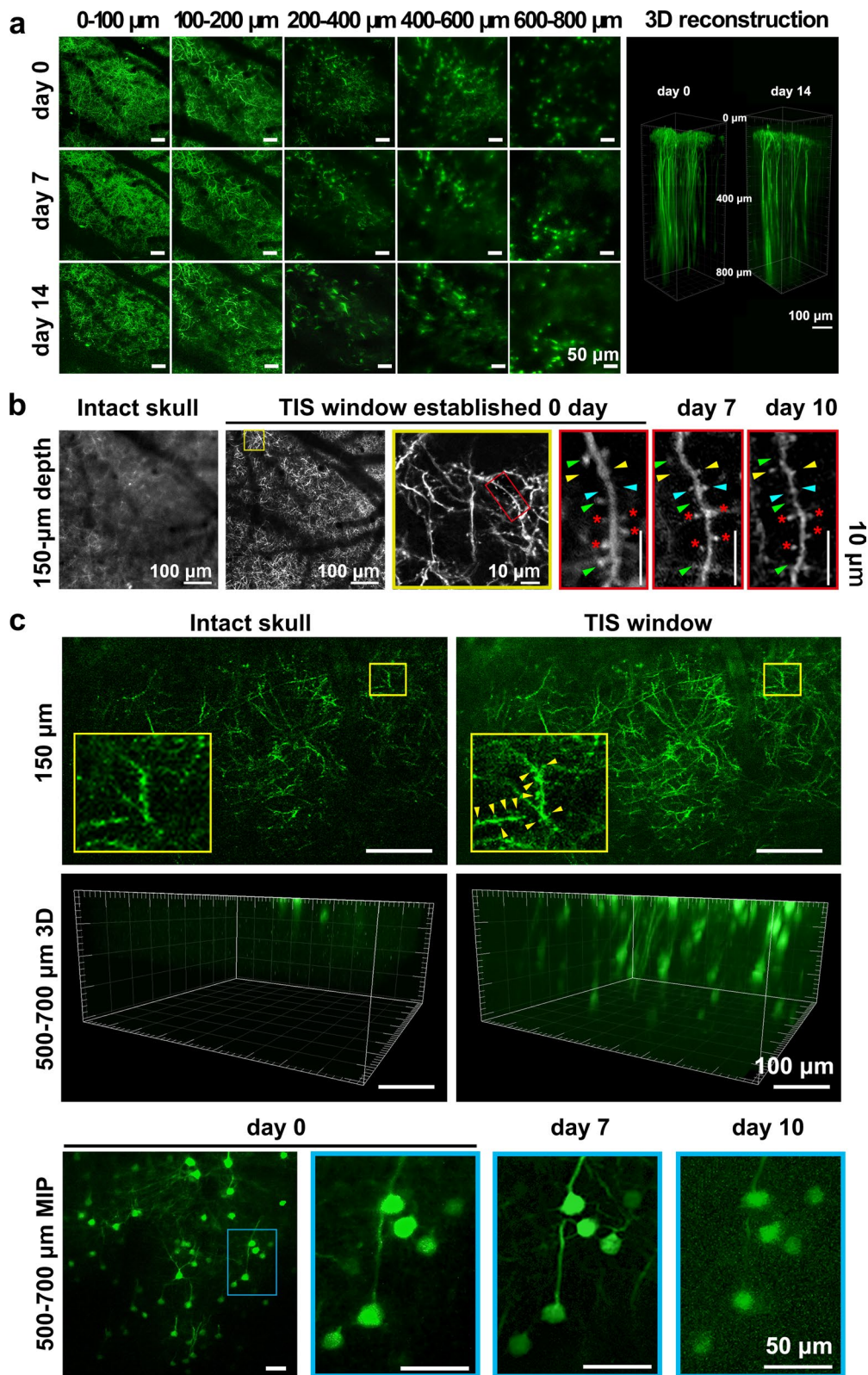
3 Discussion

What we have demonstrated in this research on in vivo TBI observation, including simultaneously discerning the movements of immune cells in different regions and perceiving random hemorrhages that occur in the bilateral cerebral cortex after acute TBI, could not be achieved before now using previous skull window techniques.
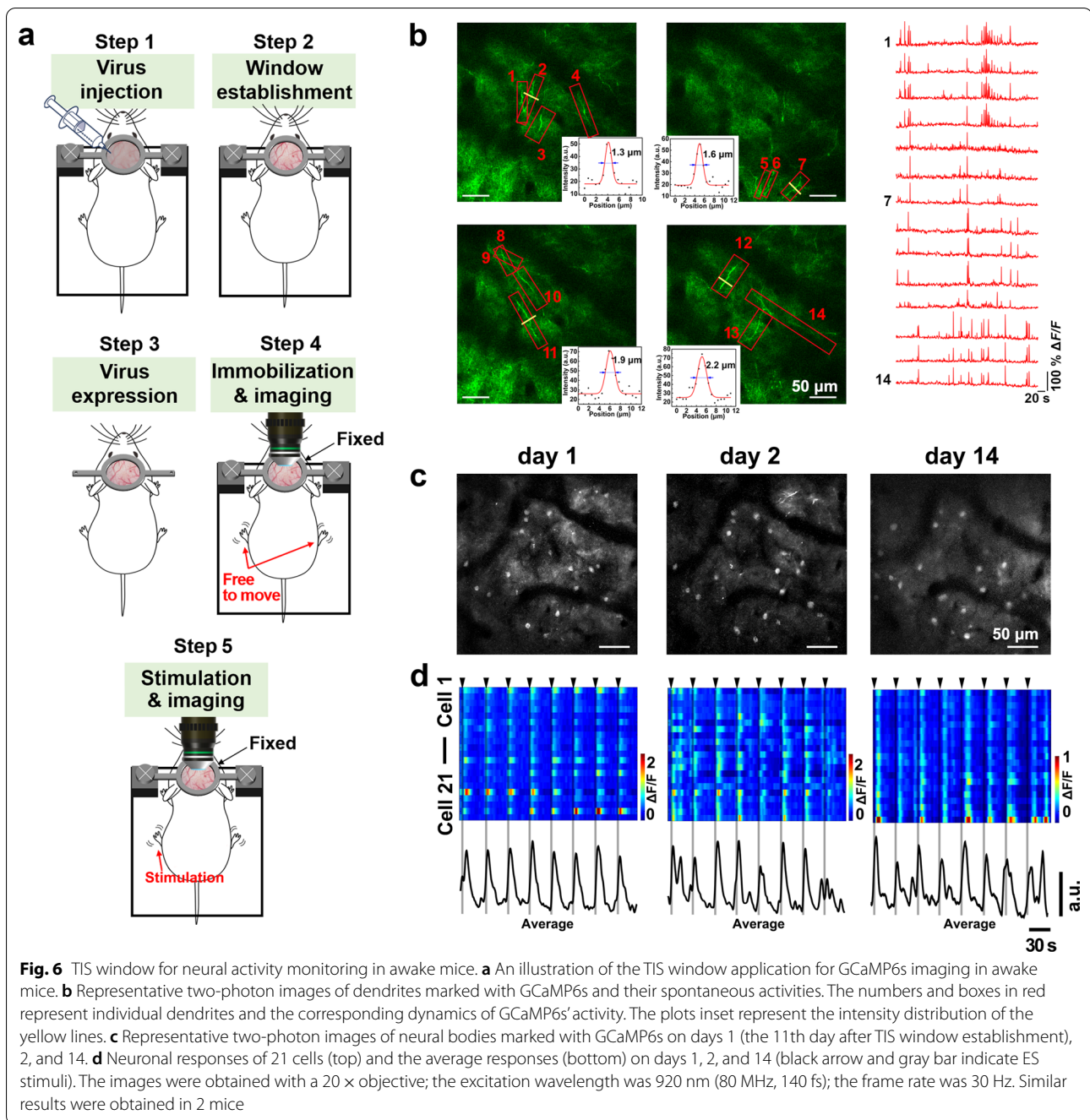
While histological data from TBI studies have provided extensive information on the spatial distribution of immune cells, as well as their state of activation, these

(See figure on next page.)

Fig. 5 TIS window for long-term neural monitoring. **a** Representative images of the two-photon cortical neural imaging of a Thy1-EGFP mouse at various depths on days 0, 7, and 14 after TIS window establishment. The axial step was set as 5 μm. **b** long-term two-photon observation of dendritic spines through the TIS window at a depth of 150 μm. Green arrows show spines that were eliminated over 10 days; yellow arrows show spines that were formed over 10 days; cyan arrows show spines that were formed and then eliminated over 10 days; asterisks show spines that persisted through 10 days. **c** Representative images of the three-photon microscopy of synaptic imaging and neural cell body long-term monitoring in deep tissue. The axial step was set as 5 μm. Yellow arrows point to the spines that were distinguishable through the TIS window. The images were obtained using a 20 × objective. The excitation wavelengths were 920 nm (80 MHz, 140 fs) and 1300 nm (400 kHz, 50 fs) for two-photon microscopy and three-photon microscopy, respectively. MIP: maximum projection. Similar results were obtained in 3 mice

Fig. 5 (See legend on previous page.)

Fig. 6 TIS window for neural activity monitoring in awake mice. **a** An illustration of the TIS window application for GCaMP6s imaging in awake mice. **b** Representative two-photon images of dendrites marked with GCaMP6s and their spontaneous activities. The numbers and boxes in red represent individual dendrites and the corresponding dynamics of GCaMP6s' activity. The plots inset represent the intensity distribution of the yellow lines. **c** Representative two-photon images of neural bodies marked with GCaMP6s on days 1 (the 11th day after TIS window establishment), 2, and 14. **d** Neuronal responses of 21 cells (top) and the average responses (bottom) on days 1, 2, and 14 (black arrow and gray bar indicate ES stimuli). The images were obtained with a 20 × objective; the excitation wavelength was 920 nm (80 MHz, 140 fs); the frame rate was 30 Hz. Similar results were obtained in 2 mice

data account for only a snapshot of the processes that are, in fact, very dynamic [40]. On the contrary, in vivo optical imaging offers detailed insights into the temporal and spatial patterns of cellular dynamics in a living brain. However, in in vivo research on TBI, both the open-skull glass window and the thinned-skull window have only delivered local views of 3–4 mm diameters, limiting their probable impact on the brain and resulting in the lack of a global field of vision [28, 29, 41]. Multiple

studies have, as a result, since revealed that TBI triggers a focal immune response [31, 32]. However, our preliminary investigation suggests that the immune response could be entirely cortical rather than limited to the vicinity of the injury. Additionally, through the TIS window, we observed the later occurrence of extensive bleeding, even in the absence of bleeding at the onset of TBI; still, the timing, location, and extent of bleeding varied greatly among individuals. Therefore, the relationship between

post-TBI bleeding and the cytodynamics of immune cells is a possible remarkable factor worth investigating in the future. Admittedly, we made only a few observations, and no biomedical conclusions can be drawn from these. Nevertheless, the TIS window does indeed provide a powerful research tool, and more experiments could be performed using the TIS window to shed light on TBI. Furthermore, according to the literature, neutrophiles appear mainly in the meninge after TBI [42–44]. Thereby, the results indicate TIS technique is also capable of monitoring life activities in meninges.

Compared to the thinned-skull window, the TIS window provides the possibility of acquiring large fields of view on the cortex. Compared to the open-skull glass window, which can also be used for large-scale observation, the TIS window holds a key advantage of maintaining the physiological/pathological environment of the brain and, therefore, can be employed for scrutiny of acute injury models. Furthermore, the mechanical resistance of the TIS technique treated skull should be better than skull removing or thinning. The open-skull glass window only leaves a cover glass above the brain, and the thinned-skull window only leaves a 25-μm-thick skull above the brain. In our case, an unpolished skull, solidified glue, and a cover glass are above the skull, thus it should protect the brain better than those surgery-based skull windows. Similarly, TIS window should do a better job of keeping the temperature of the brain unaffected by the outside world, compared to an open-skull glass window or a thinned-skull window.

The TIS window also demonstrated significant progress compared to previous skull optical clearing windows. In 2012, we firstly invented the in vivo skull optical clearing window [20], but it could be used neither for high-resolution imaging nor long-term tracking. Later, a clearing agents-based "transparent skull" technique was developed [45, 46] that can be used to monitor the cortex continuously for 1–2 months. However, it could only provide limited imaging resolution to distinguish large blood vessels due to the limited skull transparency. Since 2017 and 2018, our group has developed the "SOCW" technique[35] and the "USOCA" technique[23]. The SOCW first made it possible for mouse synaptic-resolution imaging in the superficial layer (20–80 μm) through an intact skull, but it was only suitable for slightly thinned skull adult mice and, therefore, was limited in its ability for repeatable optical clearing and imaging. The USOCA established a switchable skull optical clearing window for long-term repeatable high-resolution cortical observation. Using this approach, mice could be subjected to optical clearing and imaging once every month for over 5 months. However, the transparency of the skull would gradually diminish with the increasing regularity of treatment, leading to a limited achievable frequency and number of observations. In addition, the reagents for continuous observation had to be replaced every hour. The curable S3 in TIS technique could stabilize the transparent state of skull for a long time, thus holds the advantages of high skull optical clearing efficiency, no need for skull thinning, and more importantly, indefinite examinations of the brain over an extended period during which the skull remains transparent.

Furthermore, it is the first time that a skull optical clearing window could be used to monitor fine cortical neural structure and activities in awake mice in this research. Previously, we unveiled the SOCW, which can perform synaptic two-photon microscopy at the very surface of the cortex, but only in anesthetized mice. In the SOCW technique, the skull must be covered with glycerinum to keep it transparent. When using a water-immersed objective for two-photon imaging, a plastic wrap must be applied to separate the glycerin from water. In this case, the interface between glycerol and the plastic wrapping and the interface between plastic wrapping and water can easily be upset by any slight movement by the examined mouse, with devastating implications for imaging. On the contrary, the skull, cured S3, and coverslip remain relatively still under the TIS window approach irrespective of whether the mouse moves, significantly improving the anti-jamming ability of imaging. This property enabled the clear capturing of dendritic images in awake mice in this research.

Using advanced optical technology, it is possible to obtain good imaging results through the intact skull. For example, in Wang et al. used optimized three-photon microscopy to achieve deep-tissue calcium imaging through intact skull and achieve an imaging depth of over 500 μm [36]. Another example is that adapted optics (AO) could also be used to overcome the scattering of skull [47]. TIS window technique is possible to be combined with such advanced optical techniques to realize better imaging performance.

In the long-term calcium observation experiment, 8-week-old mice were injected with virus and the TIS window was established. 2 weeks later, the observation started and lasted for 2 weeks, at which time the mice were 3-months old. Such results suggest TIS window can work for at least 1 month and for mice smaller than 3-months old. We have tried older mice (4–6-months old). However, since the skull will become thicker as the mice grow, for older mice, although TIS window is still effective, but the transparency of the skull will be less than younger mice. Therefore, for high-resolution observation, it is better to choose mice under the age of 3 months.

Besides facilitating transcranial deep-brain imaging, the TIS approach may also enable transcranial targeted light manipulation. It has been reported that previous skull optical clearing windows are compatible with neuron dendrite or microvasculature ablation, as well as targeted photothrombotic ischemic stroke modeling [34, 35, 48, 49]. Therefore, served as an optimized skull optical clearing window, TIS window is reasonable to be used for such light manipulation. Furthermore, transcranial optogenetic neuromodulation has been explored extensively recently [50–52]. Since TIS window could reduce the light attenuation when passing through the skull, it also holds great potential to improve the efficacy of optogenetic and other light-based neuromodulation methods.

In this work, we aimed to establish a skull window to observe what is covered by the skull. Thus, we mainly paid attention to the safety of the technique on the cortex and demonstrated that TIS window would not cause cortical inflammations. Other than cortex, TIS window could also provide an opportunity to observe structures and functions in skull. Thereby, it is valuable to evaluate the impact of TIS optical clearing on the vessels and bone marrow cells in calvaria in future work.

Admittedly, TIS window still has its limitations. For example, the work time is shorter than open-skull glass window or "transparent skull" technique, which could last for months. In addition, it is not compatible with invasive GRIN lens, which is able to observe neurovascular structures and functions in deep brain [53]. Nevertheless, TIS window can be a promising alternative especially when other skull windows are not suitable, such as for large-scale high-resolution observation of acute cortical diseases.

4 Conclusions

In this investigation, we established a through-intact-skull window that enables high transparency of the skull and provides a large field of view for optical imaging without craniotomy. Using the novel TIS window, in vivo bilateral cortical visualization at single-cell resolution after acute TBI was realized for the first time. The characteristics of the TIS window were also evaluated, demonstrating its 900-μm imaging depth, dendrite spine resolution ability, long-term observation capability for weeks, and suitability for awake animals. The craniotomy-free TIS window with easy and quick steps, as a chronic skull optical clearing window, has advantages over the open-skull glass window, thinned skull window, "transparent skull" window, and skull optical clearing window, and is capable of continuous cortical monitoring at high resolution and on a centimeter-scale, with minimized influence on the brain environment. Therefore, the TIS window technique holds great potential for physiological and pathological research in brain science.

5 Materials and methods

5.1 Animals

All animal experimental procedures were performed according to animal experimental guidelines of the Experimental Animal Management Ordinance of Hubei Province, China, and the recommendations from the Huazhong University of Science and Technology, and were approved by the Institutional Animal Ethics Committee of Huazhong University of Science and Technology. 8-week-old female *Thy-1-EGFP*, *Thy-1-YFP* and *Cx3cr1^{EGFP/+}* mice were purchased from the Jackson Laboratory (Bar Harbor, ME, USA) and housed and bred in the Wuhan National Laboratory for Optoelectronics in a normal cycle (12 h light/dark). 8-week-old female wild-type *BALB/c* and C57 mice were supplied by the Wuhan University Center for Animal Experiment (Wuhan, China). Transgenic mice expressing fluorescent proteins under the influence of the Thy1 promoter (Thy1-EGFP and Thy1-YFP) were used for dendritic spine imaging, and those expressing the enhanced green fluorescent protein in microglia (Cx3cr1^{EGFP/+}) were used for microglia imaging. The wild-type *BALB/c* mice were used for non-stained cerebral blood flow/blood oxygen imaging and FITC-stained vasculature fluorescence imaging. The wild-type C57 mice were used for GCaMP6s-stained calcium imaging.

5.2 Reagents for TIS

The TIS window was established using 3 reagents: S1 (a saturated supernatant solution of 75% (vol/vol) ethanol (Sinopharm, China) and urea (Sinopharm, China) at room temperature), S2 (a high-concentration sodium dodecylbenzenesulfonate solution prepared by mixing a 0.7 M NaOH solution (Aladdin, China) with dodecylbenzenesulfonic acid (Aladdin, China) at a volume-mass ratio of 24:5), and S3 (a UV-curable adhesive, ergo 8500, Kisling, Switzerland). The refractive indices (RI) of S1, S2, and S3 are 1.399 ± 0.0008 and 1.364 ± 0.0003, and 1.513 ± 0.0016, respectively.

5.3 Establishment of the TIS window

Mice were anesthetized before the TIS window establishment. For longitudinal studies, mice were anesthetized with isoflurane (1.5%) in air. For the TBI study, mice were anesthetized with a mixture of 2% α-chloralose and 10% urethane (8 mL/kg). As shown in Additional file 1: Fig. S16a-b, to establish the TIS window, a midline

incision was made on the scalp in the direction of the sagittal suture. A holder with a 1 cm diameter hole at the center was glued to the skull, and the mouse was immobilized on a custom-built plate. Next, S1 was applied to the exposed skull for 10 min to dissociate the collagen in the skull. S1 was then removed, and S2 was smeared on the skull for 5 min to eliminate lipids in the skull. S2 removal was followed by the application of a small quantity of S3 to the skull for RI matching; S3 provided the exposed skull with a thin layer for cover, and a 1-mm coverslip was placed on the surface of S3. Lastly, the skull area was irradiated with a UV LED for 2 min, solidifying S3. Thus, the TIS window was established (Additional file 1: Fig. S15c) and used for cortical observation either immediately or later for long-term scrutiny. To measure the thickness of the cured S3, after establishment of TIS window, the cured S3 was carefully removed, along with the cover slide, from the skull, and the total thickness of S3 and cover slide was measured to be 230 μm by a vernier caliper. Then, the thickness of the cured S3 was calculated as 230 μm-150 μm (the thickness of the cover slide) = 80 μm.

As shown in Additional file 1: Fig. S15d, the TIS window provides a large field of view without craniotomy and, therefore, will not cause the immune response that is often induced by removing a large chunk of the skull. While the thinned-skull window also steers clear of inflammation, it only provides a much smaller field of view than the TIS window.

5.4 In vitro evaluation of the TIS window technique

Fresh skull samples $(0.4 \times 0.4 \text{ mm}^2)$ excised from mice were positioned in front of a spectrometer (USB4000-VIS–NIR, Ocean Inslight, USA) to evaluate the transmittance enhancement of the skull by the TIS window technique. A broad-spectrum white light source (HL-2000, Mikropack, Germany) was used to measure the transmittance spectrum (400–1000 nm) of the intact skull. The skulls were treated gradually following the steps used to establish the TIS window, and changes in the transmittance spectrum were recorded (Additional file 1: Fig. S1a).

Fresh skulls from mice were cut in half down the middle to macroscopically test the imaging quality through the TIS window. The left parts were immersed in S1, S2, and S3, followed by a 2-min UV irradiation, and the right parts were used as control. Lastly, two parts of the skulls were placed on grid paper and photographed with a camera (Additional file 1: Fig. S1b).

Fresh mice skull samples $(0.4 \times 0.4 \text{ mm}^2)$ were put on a 1951 United States Air Force (USAF) resolution test target and treated with S1, S2, S3, and UV irradiation

in sequence. A camera (AxioCamHRc, Zeiss, Germany) attached to a stereomicroscope (Zeiss Axio Zoom. V16, Zeiss, Germany) was used to capture white-light images of the skulls before and after the application of the TIS technique to quantificationally determine the increase in imaging resolution (Additional file 1: Fig. S1c).

5.5 Dual-modal imaging system for blood flow/blood oxygen imaging

A home-built dual-modal optical imaging system[54] was used to capture blood flow and blood oxygen distribution in cortical vasculature to evaluate the efficacy of the TIS window in vivo. The dual system consisted of LSCI and hyperspectral imaging (HSI). These two imaging modes share a stereoscopic microscope, and each has a light source and a detection system. For LSCI, a He–Ne laser (632.8 nm, 3 mW) beam passing through an adjustable optical attenuator was used to illuminate the areas of interest after expansion. A charge coupled device (CCD) camera (Pixefly, PCO GmBH, Germany) mounted on a stereomicroscope recorded a sequence of raw speckle images. For HSI, a ring-like LED light with a polarizer was used for illumination. A liquid crystal tunable filter (LCTF, Perkin Elmer, USA) was placed before a CCD camera in another channel to split wavelengths. The laser speckle temporal contrast[55] and multiple linear regression analysis methods[56] were used to calculate blood flow and blood oxygen, respectively.

The contrast-to-noise ratio (CNR) was used to assess the imaging quality of LSCI and was defined by the following equation [57]:

$$\text{CNR} = \frac{|C_{vessel} - C_{background}|}{\sqrt{f_{vessel}\sigma^2_{vessel} + f_{background}\sigma^2_{background}}}$$

where C_{vessel} and $C_{background}$ were the mean contrast values of the blood flow and background, respectively; σ^2_{vessel} and $\sigma^2_{background}$ were the variances in the contrast values of the blood flow and background, respectively; f_{vessel} and $f_{background}$ were the fractions of pixels classified as blood flow and background in all the selected pixels in the speckle contrast image, respectively.

5.6 TBI modeling and in vivo immune cell observation

8-week-old female BALB/c mice were anesthetized, and their scalps were cut open to expose the skull surface. Body temperature was monitored continuously with a rectal probe and maintained at 37 ± 0.5 °C. The weight-drop device consisted of a fixed plastic guide tube, 20 cm in length and centered above the skull ($- 1.0$, $- 2.0$ mm to the bregma). A 25 g weight (diameter: 3 mm) was dropped by its gravity through the guide tube. Holding

the weight with one hand immediately after the initial impact prevented a rebound impact.

After TBI, 200 µL (0.05 mg/mL) of Alexa Fluor 488 anti-mouse Ly-6G (Cat# 127626, Biolegend, USA) was injected intravenously to stain the neutrophils, followed by the TIS window establishment. A commercial fluorescence magnification microscope (Zeiss Axio Zoom. V16, numerical aperture (NA) = 0.25, Germany) was then used to continuously record the movement of immune cells on the bilateral cortex scale. The exposure time was set as 4 s per frame. After 4–6 h of monitoring, mice were sacrificed before they had the chance to wake up.

5.7 Two-photon microscopy for cerebrovascular and neural structural imaging

EGFP-expressed neuronal dendritic spines/axons/cell bodies in mice (Thy-1-EGFP) and FITC-dextran-labeled cerebral vasculature were imaged at 920 nm using a two-photon microscope (Ultima 2p; Bruker, USA) with a Ti:sapphire laser (80 MHz, Chameleon, Coherent, USA). Mice mounted with holders on their exposed skulls were placed under the microscope, and image stacks were captured utilizing a water-immersed objective (20 ×, NA = 1.00, working distance = 2 mm, Olympus). The laser power after the objective lens ranged from 10 mW (imaging at the surface) to 100 mW (imaging above a 600 µm-depth). The image stack was acquired with a depth interval of 5 µm, and pixel dwell time was 2 µs. The description of imaging depth in the Results section was from the surface of the cortex. Bright-field images of the superficial cortical vasculature were used to relocate and reimage regions of interest. While the bright-field imaging quality before skull optical clearing was limited, the low-resolution vasculature map was used for relocation.

5.8 Two-photon microscopy for calcium imaging in awake mice

Two-photon calcium imaging was performed in the somatosensory cortex region in awake mice through the TIS window. First, a small hole was drilled into the skull above S1HL (− 0.82 mm AP, 1.5 mm ML from bregma)) using a cranial drill. Second, a glass micropipette and a PicoSprizer III (Parker) were utilized to inject virus-containing GCaMP6s (rAAV-hSyn-Gcamp6s-WPRE-hGH pA, 0.3 µL) into the cortex at an angle of 45° and depth of 0.3 mm. Next, the skull hole was filled up with bone wax, and the TIS window was established.

Two weeks later, upon the full expression of the virus, mice heads with the TIS window were immobilized under the two-photon microscope for imaging, with mice free to move their pawa about. Neural calcium imaging was then conducted to record electric stimuli activities 100 µm below pia using 2PM with 30 fps. The electro-stimulation of the front paw was performed on the ipsilateral side of the recorded sensorimotor cortex as described previously [58]. The isolated pulse stimulator (AM-system, Model 2100) was used for front-paw electrical stimulation (0.2 mA, 3 Hz, biphasic ±). The stimulus included 8 trials, each trial comprising a 3 s baseline period, 3 s stimulation events, and a 24 s convalescence period for a total of 30 s.

5.9 Three-photon microscopy imaging

Mice (Thy-1-YFP) with YFP-expressing neuronal dendritic spines/axons/cell bodies were imaged for examination of the suitability of the TIS window application for long-term 3PM monitoring. We used a three-photon microscope (Ultima 2p plus; Bruker, USA) equipped with a water-immersed objective (20 ×, NA = 1.00, working distance = 2 mm, Olympus) and a 1300-nm fs laser (400 kHz, 50 fs) from a noncollinear optical parametric amplifier (Spirit-NOPA-VISIR, Spectra-Physics, USA) pumped by a regenerative amplifier (Spirit-16, Spectra-Physics, USA). Mice mounted with holders on their exposed skulls were placed under the microscope. The laser power after the objective lens ranged from 5 mW (imaging at the surface) to 50 mW (imaging above an 800 µm-depth). The image stack was acquired at a depth interval of 5 µm, and pixel dwell time was 2 µs; 4 frames were averaged. The description of imaging depth in the Results section was from the surface of the cortex.

5.10 Segmentation

Neutrophils were segmented using a simple semantic segmentation network based on dilated convolutions. The network contained four blocks of convolution, batch normalization, and ReLU layers. The filter size for each convolutional layer was 3 × 3. The calculated dice score of a softmax layer and a dice classification layer was considered the loss function. The optimizer was Adam, the epoch was 150, the initial learning rate was set to 10–3, and the minibatch size was 20.

For ground truth establishment, all datasets were labeled manually with MITK [59] based on semi-automated thresholding. The ratio of the training set to the test set was 9:1.

5.11 Cell tracking

Cells were tracked using the TrackMate plug-in in ImageJ [60] based on the segmentation results.

5.12 Safety of the TIS window

In vivo and ex vivo examinations were performed to explore the activation of microglia cells, the expression

of GFAP, and the distribution of neutrophils in the cortex through the TIS window.

The TIS window was established on the left side of the skull of Cx3cr1-GFP mice in which GFP was expressed in microglia. The mice were then placed under the two-photon microscope for 1 h of microglia monitoring. Next, the same region of interest was re-observed in vivo 48 h after the TIS window establishment because microglia activity usually reaches maximum levels 48 h after a craniotomy. After imaging, the mice were perfused and fixed with PBS and 4% paraformaldehyde (PFA, Sigma-Aldrich, USA), and their brains were subsequently extracted, placed in 4% PFA overnight for post-fixation, sliced (100 μm), and imaged with a confocal microscope (Zeiss, Germany).

Similarly, to evaluate GFAP expression, the same steps outlined above were performed, but this time the brain slices were immunohistochemically stained with anti-GFAP antibodies 10 days after the TIS window establishment and imaged with the same confocal microscope since astrocyte activity reaches a maximum at a certain time point after a craniotomy.

Given that the longest observation in this investigation lasted 21 days, microglia and GFAP expression monitoring in brain slices were conducted 21 days after the TIS window establishment.

Then, brain slices were H&E-stained and imaged using an upright microscope system (Nikon, Japan) to determine whether neutrophils penetrated the parenchyma, a sign of an inflammatory response.

Finally, the laser damage threshold through TIS window was evaluated by the two-photon microscope. The evaluation was performed by two steps. Step 1: Firstly, a two-photon image of neural dendrites was taken with normal laser power (10 mW after the objective). Secondly, turned the focus down to 700 μm deep and the laser power was set as the maximum of the laser (250 mW after the objective), then continuously scanned for 10 cycles. Thirdly, returned to the surface and took a two-photon image of the same area to evaluate if it would damage the dendrites. Step 2: used different laser power (10, 50, 100, 150, 200 mW after the objective) to focus on the brain surface and performed 10 cycles of scanning for each power to evaluate how much laser power would cause injury of the dendrites.

5.13 Data quantification

All imaging data were analyzed using the Image J software developed by the National Institutes of Health (Bethesda, Maryland). 3D image reconstruction was performed on the Imaris (Bitplane).

Supplementary Information

The online version contains supplementary material available at https://doi.org/10.1186/s43593-022-00022-2.

Additional file 1. Additional figures.

Additional file 2. Video S1. Large-scale immune cell tracking after acute TBI.

Additional file 3. Video S2. Large-scale observation of a mouse brain where hemorrhage occured after acute TBI.

Additional file 4. Video S3. Large-scale observation of a mouse brain where no hemorrhage occured after acute TBI.

Additional file 5. Video S4. Comparison on YFP-stained neuron three-photon imaging before and after TIS window establishment.

Additional file 6. Video S5. Comparison on GFP-stained neuron three-photon imaging before and after TIS window establishment.

Additional file 7. Video S6. Long-term two-photon neuron imaging through TIS window over time.

Additional file 8. Video S7. High-speed high-resolution imaging of spontaneous dendritic activity of awake mice.

Additional file 9. Video S8. Long-term observation of neural response to stimulations.

Availability of data and materials
The datasets used and/or analyzed in the current research are available upon a reasonable request to the corresponding author.

Declarations

Competing interests
The authors declare no conflict of interest.

Author details
[1]Britton Chance Center for Biomedical Photonics - MoE Key Laboratory for Biomedical Photonics, Wuhan National Laboratory for Optoelectronics

- Advanced Biomedical Imaging Facility, Huazhong University of Science and Technology, Wuhan 430074, Hubei, China. [2]Optics Valley Laboratory, Hubei 430074, China. [3]State Key Laboratory of Modern Optical Instrumentations, Centre for Optical and Electromagnetic Research, College of Optical Science and Engineering, International Research Center for Advanced Photonics, Zhejiang University, Hangzhou 310058, China. [4]Interdisciplinary Institute of Neuroscience and Technology, Department of Anesthesiology, The Second Affiliated Hospital, School of Medicine, Zhejiang University, Kaixuan Road 258th, Hangzhou 310020, China. [5]Department of Automation, Tsinghua University, Beijing 100084, China. [6]School of Optical Electronic Information - Wuhan National Laboratory for Optoelectronics - Advanced Biomedical Imaging Facility, Huazhong University of Science and Technology, Wuhan 430074, Hubei, China.

References

1. S. Lavisse et al., Increased microglial activation in patients with Parkinson disease using [18F]-DPA714 TSPO PET imaging. Parkinsonism Relat. Disord. **82**, 29–36 (2021)
2. T.G. Jovin et al., Thrombectomy for anterior circulation stroke beyond 6 h from time last known well (AURORA): a systematic review and individual patient data meta-analysis. Lancet **399**, 249–258 (2022)
3. V.L. Villemagne et al., Molecular imaging approaches in dementia. Radiology **298**, 517–530 (2021)
4. G.S. Hong, A.L. Antaris, H.J. Dai, Near-infrared fluorophores for biomedical imaging. Nat. Biomed. Eng. **1**, 0010 (2017)
5. J.L. Fan et al., High-speed volumetric two-photon fluorescence imaging of neurovascular dynamics. Nat. Commun. **11**, 6020 (2020)
6. K. Kisler et al., In vivo imaging and analysis of cerebrovascular hemodynamic responses and tissue oxygenation in the mouse brain. Nat. Protoc. **13**, 1377–1402 (2018)
7. M. Kneipp et al., Effects of the murine skull in optoacoustic brain microscopy. J. Biophotonics **9**, 117–123 (2016)
8. X.F. Fan, W.T. Zheng, D.J. Singh, Light scattering and surface plasmons on small spherical particles. Light Sci. Appl. **3**, e179 (2014)
9. A. Holtmaat et al., Long-term, high-resolution imaging in the mouse neocortex through a chronic cranial window. Nat. Protoc. **4**, 1128–1144 (2009)
10. G. Yang et al., Thinned-skull cranial window technique for long-term imaging of the cortex in live mice. Nat. Protoc. **5**, 201–208 (2010)
11. J. Fan et al., Video-rate imaging of biological dynamics at centimetre scale and micrometre resolution. Nat. Photonics **13**, 809–816 (2019)
12. S.S. Yang et al., Longitudinal in vivo intrinsic optical imaging of cortical blood perfusion and tissue damage in focal photothrombosis stroke model. J. Cerebr. Blood Flow Metab. **39**, 1381–1393 (2019)
13. T. Zhang et al., Kilohertz two-photon brain imaging in awake mice. Nat. Methods **16**, 1119–1122 (2019)
14. S.W. Cramer et al., Through the looking glass: a review of cranial window technology for optical access to the brain. J. Neurosci. Methods **354**, 109100 (2021)
15. K. Kılıç et al., Chronic cranial windows for long term multimodal neurovascular imaging in mice. Front. Physiol. (2021). https://doi.org/10.3389/fphys.2020.612678
16. T.H. Kim et al., Long-term optical access to an estimated one million neurons in the live mouse cortex. Cell Rep. **17**, 3385–3394 (2016)
17. P.J. Drew et al., Chronic optical access through a polished and reinforced thinned skull. Nat. Methods **7**, 981–984 (2010)
18. V. Coelho-Santos et al., Imaging the construction of capillary networks in the neonatal mouse brain. Proc. Natl. Acad. Sci. USA **118**, e2100866118 (2021)
19. J. Zhu et al., 1700 nm optical coherence microscopy enables minimally invasive, label-free, in vivo optical biopsy deep in the mouse brain. Light Sci. Appl. **10**, 145 (2021)
20. J. Wang et al., An innovative transparent cranial window based on skull optical clearing. Laser Phys. Lett. **9**, 469–473 (2012)
21. S. Musall et al., Single-trial neural dynamics are dominated by richly varied movements. Nat. Neurosci. **22**, 1677–1686 (2019)
22. G. Silasi et al., Intact skull chronic windows for mesoscopic wide-field imaging in awake mice. J. Neurosci. Methods **267**, 141–149 (2016)
23. C. Zhang et al., A large, switchable optical clearing skull window for cerebrovascular imaging. Theranostics **8**, 2696–2708 (2018)
24. L.G.F. Smith et al., Advanced neuroimaging in traumatic brain injury: an overview. Neurosurg. Focus **47**, E17 (2019)
25. A. Azim, B. Joseph, Traumatic Brain Injury, in *Surgical critical care therapy : a clinically oriented practical approach*. ed. by A. Salim, C. Brown, K. Inaba, M.J. Martin (Springer International Publishing, Cham, 2018), pp.1–10
26. M.C. Dewan et al., Estimating the global incidence of traumatic brain injury. J. Neurosurg. **130**, 1080–1097 (2019)
27. R.D. Dorand et al., Comparison of intravital thinned skull and cranial window approaches to study CNS immunobiology in the mouse cortex. Intravital **3**, e21978 (2014)
28. X.J. Han et al., In vivo two-photon imaging reveals acute cerebral vascular spasm and microthrombosis after mild traumatic brain injury in mice. Front. Neurosci **14**, 210 (2020)
29. H.X. Ren et al., Enriched endogenous omega-3 fatty acids in mice ameliorate parenchymal cell death after traumatic brain injury. Mol. Neurobiol. **54**, 3317–3326 (2017)
30. T.L. Roth et al., Transcranial amelioration of inflammation and cell death after brain injury. Nature **505**, 223–228 (2014)
31. K. Blennow, J. Hardy, H. Zetterberg, The neuropathology and neurobiology of traumatic brain injury. Neuron **76**, 886–899 (2012)
32. K.B. Shi, J.N. Zhang, J.F. Dong, F.D. Shi, Dissemination of brain inflammation in traumatic brain injury. Cell Mol. Immunol. **16**, 523–530 (2019)
33. E.A. Genina, A.N. Bashkatov, V.V. Tuchin, Optical clearing of cranial bone. Adv. Opt. Technol. **2008**, 267867 (2008)
34. D.Y. Li et al., Visible-near infrared-II skull optical clearing window for in vivo cortical vasculature imaging and targeted manipulation. J. Biophotonics **13**, e202000142 (2020)
35. Y.J. Zhao et al., Skull optical clearing window for in vivo imaging of the mouse cortex at synaptic resolution. Light Sci. Appl. **7**, 17153 (2018)
36. T.Y. Wang et al., Three-photon imaging of mouse brain structure and function through the intact skull. Nat. Methods **15**, 789–792 (2018)
37. N.G. Horton et al., In vivo three-photon microscopy of subcortical structures within an intact mouse brain. Nat. Photonics **7**, 205–209 (2013)
38. L. Guo et al., Dynamic rewiring of neural circuits in the motor cortex in mouse models of Parkinson's disease. Nat. Neurosci. **18**, 1299–1309 (2015)
39. T. Xu, S. Wang, R.R. Lalchandani, J.B. Ding, Motor learning in animal models of Parkinson's disease: aberrant synaptic plasticity in the motor cortex. Mov. Disord. **32**, 487–497 (2017)
40. S.M. Schwarzmaier, N. Plesnila, Contributions of the immune system to the pathophysiology of traumatic brain injury—evidence by intravital microscopy. Front. Cell. Neurosci. **8**, 358 (2014)
41. A. Mughal et al., Impaired capillary-to-arteriolar electrical signaling after traumatic brain injury. J. Cerebr. Blood Flow Metab. **41**, 1313–1327 (2021)
42. E. Sabouri et al., Neutrophil-to-lymphocyte ratio and traumatic brain injury: a review study. World Neurosurg. **140**, 142–147 (2020)
43. M.W. Buckley, D.B. McGavern, Immune dynamics in the CNS and its barriers during homeostasis and disease*. Immunol. Rev. **306**, 58–75 (2022)
44. M.V. Russo, L.L. Latour, D.B. McGavern, Distinct myeloid cell subsets promote meningeal remodeling and vascular repair after mild traumatic brain injury. Nat. Immunol. **19**, 442–452 (2018)
45. A. Steinzeig, D. Molotkov, E. Castren, Chronic imaging through "transparent skull" in mice. PLoS ONE **12**, e0181788 (2017)
46. L. Pinto et al., Task-dependent changes in the large-scale dynamics and necessity of cortical regions. Neuron **104**, 810–824 (2019)
47. Z. Qin et al., Deep tissue multi-photon imaging using adaptive optics with direct focus sensing and shaping. Nat. Biotechnol. (2022). https://doi.org/10.1038/s41587-022-01343-w
48. Z.W. Hu et al., In vivo tissue optical clearing assisted through-skull targeted photothrombotic ischemic stroke model in mice. J. Biomed. Opt. **27**, 065001 (2022)
49. D.Y. Li et al., Optical clearing imaging assisted evaluation of urokinase thrombolytic therapy on cerebral vessels with different sizes. Biomed. Opt. Express **13**, 3243–3258 (2022)
50. X. Wu et al., Tether-free photothermal deep-brain stimulation in freely behaving mice via wide-field illumination in the near-infrared-II window. Nat. Biomed. Eng. **6**, 754–770 (2022)

51. R. Chen et al., Deep brain optogenetics without intracranial surgery. Nat. Biotechnol. **39**, 161–164 (2021)

52. S. Chen et al., Near-infrared deep brain stimulation via upconversion nanoparticle-mediated optogenetics. Science **359**, 679–683 (2018)

53. Z. Qin et al., Adaptive optics two-photon endomicroscopy enables deep brain imaging at synaptic resolution over large volumes. Sci. Adv. (2020). https://doi.org/10.1126/sciadv.abc6521

54. W. Feng et al., Comparison of cerebral and cutaneous microvascular dysfunction with the development of type 1 diabetes. Theranostics **9**, 5854–5868 (2019)

55. M. Draijer, E. Hondebrink, T.V. Leeuwen, W. Steenbergen, Review of laser speckle contrast techniques for visualizing tissue perfusion. Lasers Med. Sci. **24**, 639 (2009)

56. F. Wei et al., Lookup-table-based inverse model for mapping oxygen concentration of cutaneous microvessels using hyperspectral imaging. Opt. Express **25**, 3481–3495 (2017)

57. J. Wang et al., Tissue optical clearing window for blood flow monitoring. IEEE J. Select. Topics Quantum Electron. **20**, 92–103 (2013)

58. I.R. Winship, T.H. Murphy, In vivo calcium imaging reveals functional rewiring of single somatosensory neurons after stroke. J. Neurosci. **28**, 6592–6606 (2008)

59. I. Wolf et al., The medical imaging interaction toolkit. Med. Image Anal. **9**, 594–604 (2005)

60. J.Y. Tinevez et al., TrackMate: an open and extensible platform for single-particle tracking. Methods **115**, 80–90 (2017)